Strain Reversal in Actuated Origami Structures

Steven W. Grey,* Fabrizio Scarpa, and Mark Schenk
Bristol Composites Institute (ACCIS), Department of Aerospace Engineering, University of Bristol, BS8 1TR Bristol, United Kingdom

(Received 14 December 2018; published 10 July 2019)

Origami in engineering is gaining interest for its potential as deployable or shape-adaptive structures. Practical systems could employ a network of actuators distributed across the structure to induce these deformations. Selecting the actuator locations requires an understanding of how the effect of a single actuator propagates spatially in an origami structure. We combine experimental results, finite element analysis, and reduced-order bar-and-hinge models to show how a localized static actuation decays elastically in Miura-ori tubes and sheets. We observe a strain reversal, before the origami structure springs back to the initial configuration further away from the point of actuation. The strain reversal is the result of bending of the facets, while the spring back requires in-plane facet deformations.

DOI: 10.1103/PhysRevLett.123.025501

Engineering applications of origami, as deployable or shape-adaptive structures, are unfolding across various fields [1–3]. It is therefore important to consider how such origami structures can be designed to achieve a defined shape. Uniform self-folding across a sheet of origami has been investigated previously [4]; instead, we aim to exploit a network of distributed actuators to reconfigure an origami structure. This allows for an adaptive system, which is reconfigurable into a range of 3D configurations from a single flat sheet. The selection of the size and location of such actuators, e.g., fluidic pressure [5] or shape memory materials [6], is driven by the mechanical response of the structure.

The simplest model to capture the mechanics of origami, rigid origami [7], represents the folds as perfect hinges and the material between the folds, the facets, as infinitely stiff. This kinematic understanding of origami shows that the Miura-ori [8], a common unit cell in tessellated origami, has a single degree of freedom, and drives the models showing the global behavior of Miura-ori structures [9,10]. However, simple experimentation with a paper model of a Miura-ori structure shows that, in practice, it does not possess a single degree of freedom; a local actuation, e.g., the opening of a single fold, does not propagate evenly throughout the structure. Instead, it decays away from the source, because the facets are able to deform; see Fig. 1. The aim of this Letter is to understand the effect of these facet deformations on the elastic decay of a localized actuation in an origami structure. This understanding is a step towards designing actuated origami structures, for either deployment or transformation into another 3D configuration.

Localization of an actuation can be captured by augmenting rigid origami with a pseudofold across the short diagonal of the facets to represent their bending [11], which increases the number of degrees of freedom. Adding a stiffness to the folds and pseudofolds transforms the Miura-ori from a mechanism into a structure [12]. Bar-and-hinge models offer an efficient approach to capture the structural behavior of origami [3,11,13,14]. In these models bars are placed along the fold lines and across the facet diagonals, to model the in-plane facet deformations, and the fold and facet bending stiffness are represented by hinges along the bars. These models have been extended to nonlinear analyses, such as the open-access software MERLIN2 [15], which is used in the current work.

For a higher fidelity investigation of the response of origami to a localized actuation, finite element analysis (FEA) may be used. Using shell elements to model the facets, FEA has been applied to linear-elastic static problems [16,17], as well as analyses involving plastic deformations [18,19]. The folds are generally modeled as smooth curved sections, or by shell elements connected at a fixed angle. FEA provides insight into the behavior of origami structures, but reduced-order models, such as the bar-and-hinge models, are often preferable for providing a physical understanding [3,9].

Another approach is to exploit the translational symmetry of origami structures such as the Miura-ori and employ a Bloch wave analysis, which is typically used to

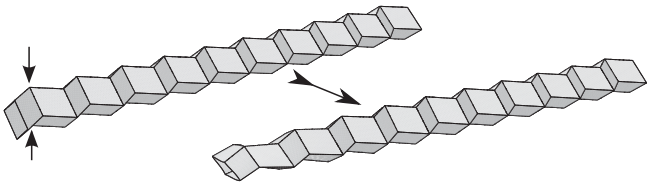

FIG. 1. A localized actuation, here compressing a unit cell, at one end of a Miura-ori tube propagates along its length. The deformation elastically decays away from the source, eventually returning to the unperturbed shape. This elastic decay is a result of facet deformations, which alter the unit cell kinematics.

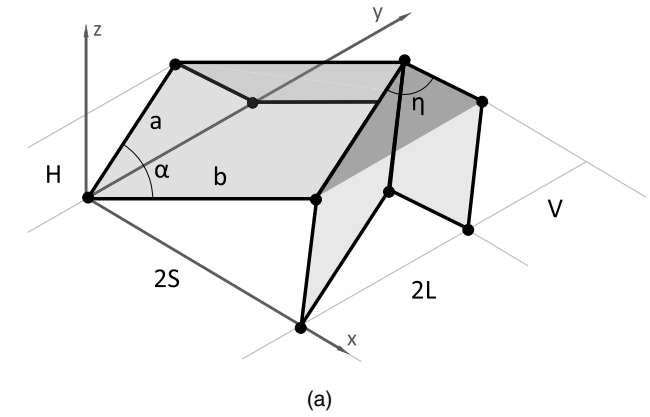

(a)

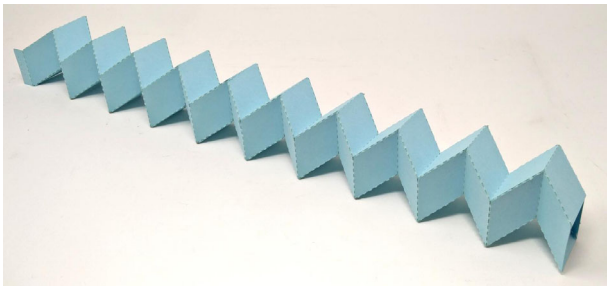

(b)

FIG. 2. (a) Geometric parameters of a Miura-ori unit cell. Angle η is used to characterize the unit cell deformation. (b) Physical model of Miura-ori tube used in the experiments.

analyze wave propagation in periodic structures [20]. Evans *et al.* [21] use a similar technique to investigate the decay of local perturbations in Miura-ori sheets. The effect of a local perturbation is related to its magnitude and the unit cell geometry, where the facets are permitted to bend around the short diagonal, but the effect of in-plane stiffness is neglected. In this Letter we challenge the assumption that the bending of the facets, and opening and closing of the folds, can fully capture how a localized actuation decays. Instead, we shall demonstrate that it is also important to incorporate the in-plane deformation of the facets, using experimental, FEA, and reduced-order models.

Local actuation of Miura-ori tube.—We simplify the spatial decay of a localized actuation to a single dimension by considering Miura-ori tubes [3,22]. The local actuation is here taken as a compression of a unit cell at one end of the tube, by moving the top and bottom vertices towards each other; see Fig. 1. Different methods of actuation, such as opening various combinations of folds, were found to give equivalent responses. Squeezing was selected for ease of implementation in the experiments and reduced-order models. The elastic decay of the actuation is captured by the angle η between the parallel folds; see Fig. 2. The unit cell deformation is normalized as $\hat{\eta}$,

$$\hat{\eta} = \frac{\eta - \eta_0}{\eta_{\max} - \eta_0}, \tag{1}$$

with initial configuration η_0 and maximum deformed configuration along the tube $\eta_{\max}$.

Experimental samples are constructed from card material (300 gsm Canford) with a thickness of 0.37 mm. Each tube consists of 10 unit cells, with dimensions $a = b = 30$ mm and angle $\alpha = 60°$, as defined in Fig. 2. The fold lines are perforated using a laser cutter (2 mm cuts separated by 2 mm material). Each half of the tube is folded separately, and bonded together using double-sided adhesive tape attached to tabs. The finished tube is fully compressed, then fully extended, in the x direction and allowed to return back to a natural rest state, with $\eta_0 \approx 104°$. Thus all folds in the tube undergo two full cycles of 180° from flat to folded and back, before being allowed to rest. The initial rest state varies slightly between samples, but this has limited effect on the observed response, as evidenced by the narrow band of experimental scatter in Fig. 3. The tubes are then placed horizontally, to eliminate the effects of gravity. The unit cell on one end is compressed symmetrically by approximately 10 mm, actuating the tube in a manner consistent with Fig. 1. The deformed geometry is captured using a 3D laser scanner, and the resulting point cloud is processed to extract the fold lines, vertices, and $\hat{\eta}$ along the tube [23]. Three different samples of the tubes were manufactured, as shown in Fig. 2(b).

The finite element model is implemented in ABAQUS/STANDARD. The facets are meshed using S4R shell elements, and the folds are modeled using torsional springs (CONN3D2) between coincident nodes. For further details of the finite element modeling, see Supplemental Material [24]. The facet material properties were determined from tensile tests of the card material. The card material has a dominant grain direction, and is therefore specially orthotropic. However, FEA models using corresponding isotropic facet properties showed similar responses, and thus the equivalent isotropic Young's modulus 3750 MPa and Poisson's ratio $\nu = 0.26$ were used. An average fold stiffness $k_F = 0.1$ N/rad (per unit length of fold) was determined using two methods, a global compression of the tubes [23] and single fold testing (see Supplemental Material [24]). The fold stiffness was found not to vary significantly with the orientation with respect to the grain of the card, likely due to the removal of a significant portion of the material at the fold in the perforation process.

For both the FEA model and the experimental results, the angles η are calculated by fitting a straight line to the points which are on the front and rear parallel folds. The angle between these lines is taken as η.

As seen in Fig. 3, both experimental and FEA results show an elastic decay of the local actuation along the length of the tube. Notably, a strain reversal is observed, indicated by negative values for $\hat{\eta}$, where the unit cell deformation is of the opposite sense to the actuation. Towards the end of the tube $\hat{\eta}$ returns to zero, i.e., the undeformed configuration, here referred to as spring back. These effects, despite

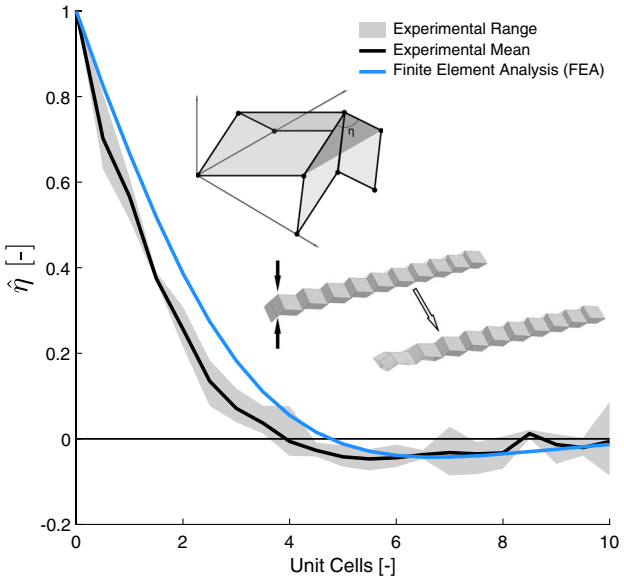

FIG. 3. Comparison of experimental results and numerical models. The unit cell deformation $\hat{\eta}$ is plotted along the length of the tube. Both experimental and FEA results show a strain reversal of the unit cells ($\hat{\eta} < 0$), before springing back to the original configuration ($\hat{\eta} = 0$).

their small magnitude, are measurable and perceptible in the physical models. The difference between the FEA model and the experimental model could be due to uncertainty in the experimentally obtained linear fold stiffness used in the torsional springs in the FEA model. This study focuses on understanding the trends and contributing factors behind the mechanical response observed experimentally and captured in the FEA models. To gain a better physical insight into the deformations, we therefore analyze the Miura-ori tube using a reduced-order bar-and-hinge model.

The bar-and-hinge models for origami structures allow the in-plane, facet bending, and fold stiffness to be varied independently [11,13]. Models with a single pseudofold across the short diagonal of a facet consist of four nodes, joined together by five bars, and are referred to as N4B5. The in-plane deformations can be captured more accurately by placing bars (and thus pseudofolds) across both diagonals and adding a node at the intersection, resulting in an N5B8 model [13]. Figure 4 shows the result of two bar-and-hinge types, the nonlinear N5B8 implementation in MERLIN2 [15] and a linear N4B5 model [11], which represent two levels of simplification from the FEA. A challenge in using reduced-order models is determining suitable equivalent material properties. Both models calculate the facet bending stiffness according to the empirical equations by Filipov *et al.* [13]. For the linear N4B5 model the in-plane stiffness was calibrated to produce a realistic response, and due to its linearity the actuation magnitude is $1/1000$ of the unit cell height H. Both reduced-order models accurately capture the behavior exhibited in the FEA model. Hence, the rest of the results reported in this

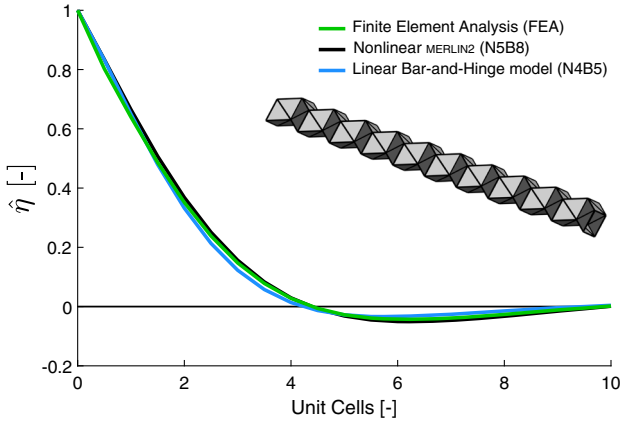

FIG. 4. The nonlinear MERLIN2 and linear bar-and-hinge model capture the behavior accurately compared to FEA, where $k_F = 0.1$ N/rad, $k_B = 1.3$ N/rad, and $k_S = 1.0$ N/m.

Letter use the linear N4B5 model, restricting the direct applicability to small changes in geometry.

Effect of stiffness on local actuation.—Using this model, we explore the effect of the different stiffness components (bar stiffness k_S, facet bending stiffness k_B, and fold stiffness k_F) on the observed elastic decay of the Miura-ori tube, and specifically its strain-reversal and spring-back features. In the finite element model the facet in-plane and bending stiffness are intrinsically linked through the elastic properties (E, ν) and facet geometry (thickness t, dimensions a, b, angle α). Here we vary the three stiffness components of the reduced-order model independently, and report the results in terms of the ratio μ_{FB} of the fold and facet bending stiffness,

$$\mu_{FB} = \frac{k_F}{k_B} = k_F \frac{12(1-\nu^2)d}{Et^3(0.55 - 0.42\frac{2\alpha}{\pi})} \left(\frac{t}{d}\right)^{1/3}, \quad (2)$$

and the ratio μ_{FS} of the fold and facet in-plane stiffness,

$$\mu_{FS} = \frac{k_F}{k_S} = \frac{k_F}{EA}, \quad (3)$$

with the length of the short diagonal d, thickness of the facets t, and the bar area A. The facet bending stiffness k_B is based on the expression from Filipov *et al.* [13]. Lechenault *et al.* [25] introduced an "origami length scale" as the ratio of material flexural stiffness and the fold stiffness, but we here use μ_{FB} to also account for the facet geometry.

To understand the effect of the stiffness ratios, μ_{FB} and μ_{FS}, three cases are considered. First, the bending and in-plane stiffness of the facets are separated, using Lagrange multipliers to constrain facets to be inextensible or remain planar. Next, we show the transition from inextensible facets to a tube with physical properties, to highlight how a realistic response to a local actuation is a combination of these two special cases.

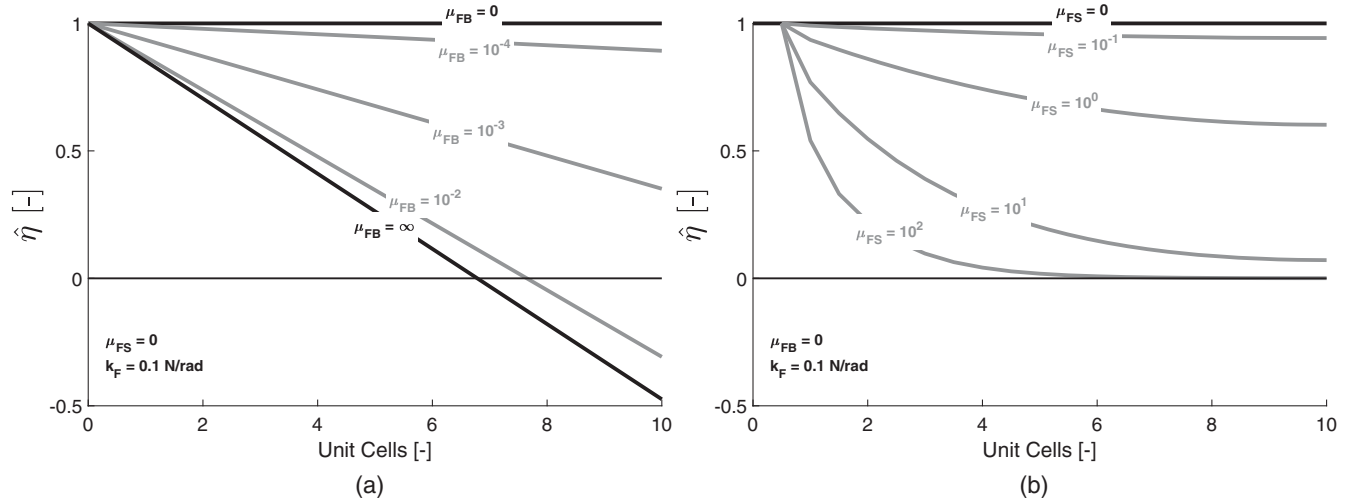

FIG. 5. Effect of stiffness parameters on localization of actuation in a Miura-ori tube. (a) Ratio μ_{FB} of fold and bending stiffness is varied for infinite in-plane stiffness ($k_S = \infty$). (b) Ratio μ_{FS} of fold and in-plane stiffness is varied for flat facets ($k_B = \infty$).

For an infinite in-plane facet stiffness ($\mu_{FS} = 0$), the folding/bending ratio μ_{FB} is varied for a fixed value of $k_F = 0.1$ N/rad, in Fig. 5(a). Rigid origami is represented by $\mu_{FB} = 0$, and $\mu_{FB} = \infty$ corresponds to a situation where the pseudofolds capturing the bending of the facets are perfect hinges. For the full range of $\mu_{FB} = 0$ to $\mu_{FB} = \infty$, the decay of the localized actuation is linear. Increasing μ_{FB}, effectively reducing the bending stiffness of the facets, causes the local actuation to linearly decay within a shorter length; for sufficiently high μ_{FB}, a strain reversal is observed. Therefore, strain-reversal can occur without in-plane facet deformations.

Next, the facets are constrained to remain planar ($\mu_{FB} = 0$), and the effect of the in-plane facet stiffness is investigated by varying μ_{FS}. Rigid origami is represented by $\mu_{FS} = 0$, and $\mu_{FS} \to \infty$ corresponds to facets with no in-plane stiffness. The results in Fig. 5(b) show a decay towards the initial state. For sufficiently long tubes the actuation will decay back to the initial state for all non-zero μ_{FS} (see Supplemental Material [24]). However, no value of μ_{FS} exhibits a strain reversal.

A physical structure is a combination of these two cases, including both facet bending and in-plane facet deformations. Increasing μ_{FS} for a fixed ratio of fold and facet bending stiffness $\mu_{FB} \approx 0.1$, effectively decreasing the in-plane facet stiffness from infinity, shows a transition from a linear elastic decay to a response observed experimentally; see Fig. 6. The fixed value of μ_{FB} is derived from experimental testing of the card used in the experiments and equations outlined by Filipov *et al.* [13]; see Supplemental Material [24] for further details, including Refs. [11,13,15,23,26–28]. Therefore, it may be observed that the bending of the facets causes a strain reversal in the locally actuated Miura-ori tubes, with a spring back to the initial condition caused by the in-plane deformations. Of note is the sensitivity to changes in the ratios μ_{FB} and μ_{FS} around the representative experimental values of 0.1. Figure 5(a) shows how μ_{FB} is insensitive to changes of an order of magnitude. In contrast, μ_{FS} in Fig. 5(b) shows a much greater sensitivity, suggesting that the effect of the in-plane stiffness is more significant in the response to a local actuation of the tubular origami structures. For a comparison of the strain energy associated with the in-plane and bending strains, see Supplemental Material [24], which includes Ref. [29].

For Figs. 5 and 6 the fold stiffness is kept constant, $k_F = 0.1$ N/rad, and the ratios μ_{FB} and μ_{FS} are changed by altering the facet bending and in-plane stiffness, respectively. Changing the fold stiffness 2 orders of magnitude either way from a realistic value yields a near-identical response; therefore, these conclusions can be considered robust for a realistic fold stiffness.

Discussion.—Our results offer an insight into the behavior of physical origami structures with embedded, localized

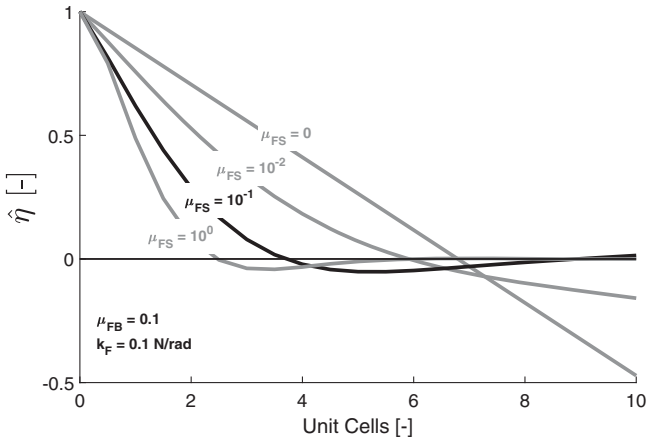

FIG. 6. A transition from infinite to realistic in-plane facet stiffness, where $\mu_{FB} = 0.1$ and $k_B = 0.1$ N/rad.

actuation. We observe an elastic decay with a "strain reversal" where an actuation causes a deformation of the opposite sense elsewhere in the structure, before returning to the undeformed configuration. This result challenges the assumption of a simple exponential decay in modeling tessellated origami structures [21]. Furthermore, incorporating the in-plane facet stiffness is shown to be critical in capturing the observed response of origami structures.

Using a reduced-order bar-and-hinge model, the contributions of the fold stiffness (k_F), facet bending stiffness (k_B), and in-plane facet stiffness (k_S) could be explored separately. The elastic decay was characterized using two stiffness ratios: $\mu_{FS} = k_F/k_S$ and $\mu_{FB} = k_F/k_B$. For fixed ratios, varying the stiffness does not change the response to a local actuation; however, it would affect the amount of energy an actuator would need to impart to achieve a desired deformation. For Miura-ori tubes the elastic decay is dominated by μ_{FS}.

By exploring distributed actuation we extend our ability to design engineering origami systems, compared to origami structures where all of the folds are actuated simultaneously. This would, for instance, enable reconfigurable structures which can attain multiple configurations, or the design of deployable structures with elastic hinges to control the deployment speed.

The current work has focused on actuating origami structures at a single location, and future work will explore the interaction of multiple actuators distributed across the structure. The work may also be extended to nonrigid foldable patterns, dynamic actuation, power-limited actuators, as well as development of physical prototypes.

Data are available at the University of Bristol data repository, data.bris, at [30].

This work was supported by the Engineering and Physical Sciences Research Council (EPSRC) through the ACCIS Doctoral Training Centre (Grant No. EP/G036772/1). We thank Professor Paul Weaver for the insightful suggestion of comparing the Miura-ori tubes to the model of a beam on an elastic foundation, which is elaborated in the Supplemental Material [24].

*steven.grey@bristol.ac.uk

[1] K. Kuribayashi, K. Tsuchiya, Z. You, D. Tomus, M. Umemoto, T. Ito, and M. Sasaki, Self-deployable origami stent grafts as a biomedical application of Ni -rich TiNi shape memory alloy foil, Mater. Sci. Eng. A **419**, 131 (2006).

[2] Z. Song, T. Ma, R. Tang, Q. Cheng, X. Wang, D. Krishnaraju, R. Panat, C. K. Chan, H. Yu, and H. Jiang, Origami lithium-ion batteries, Nat. Commun. **5**, 3140 (2014).

[3] E. T. Filipov, T. Tachi, and G. H. Paulino, Origami tubes assembled into stiff, yet reconfigurable structures and metamaterials, Proc. Natl. Acad. Sci. U.S.A. **112**, 12321 (2015).

[4] C. D. Santangelo, Extreme mechanics: self-folding origami, Annu. Rev. Condens. Matter Phys. **8**, 165 (2017).

[5] H. Sane, P. Bhovad, and S. Li, Actuation performance of fluidic origami cellular structure: a holistic investigation, Smart Mater. Struct. **27**, 115014 (2018).

[6] E. A. Peraza-Hernandez, D. J. Hartl, R. J. Malak, Jr., and D. C. Lagoudas, Origami-inspired active structures: a synthesis and review, Smart Mater. Struct. **23**, 094001 (2014).

[7] T. Tachi, Simulation of rigid origami, in *Origami 4* (A. K. Peters/CRC Press, Boca Raton, 2009), pp. 175–187.

[8] K. Miura, Method of packaging and deployment of large membranes in space, The Institute of Space and Astronautical Science report, Technical Report, The Institute of Space and Astronautical Science, 1985, https://repository.exst.jaxa.jp/dspace/handle/a-is/7293.

[9] M. Schenk and S. D. Guest, Geometry of Miura-folded metamaterials, Proc. Natl. Acad. Sci. U.S.A. **110**, 3276 (2013).

[10] Z. Y. Wei, Z. V. Guo, L. Dudte, H. Y. Liang, and L. Mahadevan, Geometric Mechanics of Periodic Pleated Origami, Phys. Rev. Lett. **110**, 215501 (2013).

[11] M. Schenk and S. D. Guest, Origami folding: a structural engineering approach, in *Origami 5: Fifth International Meeting of Origami Science, Mathematics, and Education* (CRC Press, Boca Raton, 2011), pp. 291–304.

[12] V. Brunck, F. Lechenault, A. Reid, and M. Adda-Bedia, Elastic theory of origami-based metamaterials, Phys. Rev. E **93**, 033005 (2016).

[13] E. Filipov, K. Liu, T. Tachi, M. Schenk, and G. Paulino, Bar and hinge models for scalable analysis of origami, Int. J. Solids Struct. **124**, 26 (2017).

[14] K. Liu and G. H. Paulino, Nonlinear mechanics of non-rigid origami: an efficient computational approach, Proc. R. Soc. A **473**, 20170348 (2017).

[15] K. Liu and G. H. Paulino, Highly efficient nonlinear structural analysis of origami assemblages using the MERLIN2 software, in *The proceedings from the seventh meeting of Origami, Science, Mathematics and Education* (Tarquin, St Albans, 2018).

[16] S. Liu, G. Lu, Y. Chen, and Y. W. Leong, Deformation of the Miura-ori pattered sheet, Int. J. Mech. Sci. **99**, 130 (2015).

[17] J. Gattas and Z. You, Quasi-static impact of indented foldcores, Int. J. Solids Struct. **53**, 80 (2015).

[18] J. Ma and Z. You, Energy absorption of thin-walled square tubes with a prefolded origami pattern—Part 1: geometry and numerical simulation, J. Appl. Mech. **81**, 011003 (2013).

[19] M. Schenk, S. D. Guest, and G. J. McShane, Novel stacked folded cores for blast-resistant sandwich beams, Int. J. Solids Struct. **51**, 4196 (2014).

[20] P. P. Pratapa, P. Suryanarayana, and G. H. Paulino, Bloch wave framework for structures with nonlocal interations: Application to the design of origami acoustic metamaterials, J. Mech. Phys. Solids **118**, 115 (2018).

[21] A. A. Evans, J. L. Silverberg, and C. D. Santangelo, Lattice mechanics of origami tessellations, Phys. Rev. E **92**, 013205 (2015).

[22] E. T. Filipov, G. H. Paulino, and T. Tachi, Origami tubes with reconfigurable polygonal cross-sections, Proc. R. Soc. A **472**, 20150607 (2016).

[23] S. Grey, F. Scarpa, and M. Schenk, Local actuation of tubular origami, in *The proceedings from the seventh meeting of Origami, Science, Mathematics and Education* (Tarquin, St Albans, 2018).

[24] See Supplemental Material at http://link.aps.org/supplemental/10.1103/PhysRevLett.123.025501 for further details of the models used, characterisation of the experimental material, sensitivity analysis of the conclusions, and a comparison to the system of a beam on an elastic foundation.

[25] F. Lechenault, B. Thiria, and M. Adda-Bedia, Mechanical Response of a Creased Sheet, Phys. Rev. Lett. **112**, 244301 (2014).

[26] E. Boatti, N. Vasios, and K. Bertoldi, Origami metamaterials for tunable thermal expansion, Adv. Mater. **29**, 1700360 (2017).

[27] F. Lopez Jimenez and S. Pellegrino, Folding of fiber composites with a hyperelastic matrix, Int. J. Solids Struct. **49**, 395 (2012).

[28] J. P. Den Hartog, *Advanced Strength of Materials* (McGraw-Hill Book Company Inc., New York, 1952).

[29] C. R. Calladine, *Theory of Shell Structures* (Cambridge University Press, New York, 1983).

[30] https://data.bris.ac.uk/data/dataset/3ue314qgo62302p5ou36zyeckx.